

RESEARCH LETTER

10.1002/2016GL067926

Key Points:

- High-resolution simulations show intense submesoscale upwelling in anticyclones
- The upwelling can drive a large increase in biological productivity
- The cause is symmetric instability that is not included in current nutrient budgets

Supporting Information:

- Movie S1
- Figure S1
- Figure S2
- Supporting Information S1

Correspondence to:

L. Brannigan,
liam.brannigan@misu.su.se

Citation:

Brannigan, L. (2016), Intense submesoscale upwelling in anticyclonic eddies, *Geophys. Res. Lett.*, 43, 3360–3369, doi:10.1002/2016GL067926.

Received 24 JAN 2016

Accepted 3 MAR 2016

Accepted article online 9 MAR 2016

Published online 4 APR 2016

©2016. The Authors.

This is an open access article under the terms of the Creative Commons Attribution License, which permits use, distribution and reproduction in any medium, provided the original work is properly cited.

Intense submesoscale upwelling in anticyclonic eddies

L. Brannigan^{1,2}
¹Atmospheric, Oceanic and Planetary Physics, University of Oxford, Oxford, UK, ²National Oceanography Centre, University of Southampton, Southampton, UK

Abstract Observations from around the global ocean show that enhanced biological activity can be found in anticyclonic eddies. This may mean that upwelling of nutrient-rich water occurs within the eddy, but such upwelling is not captured by models that resolve mesoscale processes. High-resolution simulations presented here show intense submesoscale upwelling from the thermocline to the mixed layer in anticyclonic eddies. The properties of the upwelling are consistent with a process known as symmetric instability. A simple limiting nutrient experiment shows that this upwelling can drive much higher biological activity in anticyclonic eddies when there is a high nutrient concentration in the thermocline. An estimate for the magnitude of upwelling associated with symmetric instability in anticyclonic eddies in the Sargasso Sea shows that it may be of comparable magnitude to other processes, though further work is required to understand the full implications for basin-scale nutrient budgets.

1. Introduction

A major oceanographic challenge is that nutrient budgets across wide regions of the ocean do not close as in situ estimates of biological productivity are greater than the estimated rate of nutrient supply required for such productivity [Shulenberger and Reid, 1981; Jenkins and Goldman, 1985], and the estimated combined contribution from wintertime convection [Michaels et al., 1994], diapycnic diffusion [Dietze et al., 2004], Ekman upwelling [Williams and Follows, 1998], and nitrogen fixation [Gruber and Sarmiento, 1997] among other processes is insufficient to close regional budgets [Williams and Follows, 2011]. It is thought that mesoscale eddies may play an important role in closing such budgets [e.g., McGillicuddy et al., 2007]. Observations from around the global ocean show that greatly enhanced chlorophyll-a can be observed in anticyclonic eddies compared to surrounding waters [Yentsch and Phinney, 1985; Crawford et al., 2007; Hansen et al., 2010; Lehahn et al., 2011; Godø et al., 2012; Gaube et al., 2013]. If the observed high biomass concentration reflects high biological productivity within the eddy rather than stirring of a large-scale gradient in surface chlorophyll [Martin, 2003], there must be upwelling of nutrient-rich water within the eddy.

Mesoscale eddy-resolving simulations may include a number of different processes that supply the euphotic zone with nutrients beyond the vertical velocities associated with the formation and advection of the eddies. These processes include deeper mixed layers [Dewar, 1986], frictional decay [Franks et al., 1986], upwelling due to Ekman pumping induced by a relative wind stress [Dewar and Flierl, 1987] or the convergences in the Ekman transport induced by gradients in the vertical component of relative vorticity [Stern, 1965; Mahadevan et al., 2008]. However, ocean models that resolve mesoscale eddies and include these processes find only a minor increase in simulated productivity [Eden and Dietze, 2009].

As part of the Ocean Surface Mixing - Ocean Submesoscale Interaction Study (OSMOSIS), Brannigan et al. [2015] perform simulations of the seasonal cycle of submesoscale flows. A consistent feature of the simulations is the presence of ageostrophic submesoscale filaments inside mesoscale anticyclonic eddies. The simulations presented here investigate the dynamical properties of these filaments. The analysis shows that intense submesoscale upwelling from the thermocline to the mixed layer occurs in wind-forced anticyclonic eddies. The dynamical process driving this upwelling is found to be symmetric instability. A limiting nutrient experiment shows that this upwelling leads to an increase in net biological productivity compared to experiments where the upwelling is poorly resolved. The experimental setup is outlined in section 2, the filamentary upwelling is described in section 3, and the limiting nutrient experiment is carried out and considered in section 4. The implications and limitations of the results are discussed in section 5.

2. Experiment Setup and Methods

2.1. Numerical Overview

Numerical simulations are carried out using the high-resolution Massachusetts Institute of Technology general circulation model (MITgcm) [Marshall *et al.*, 1997] in a hydrostatic configuration analogous to the wind-forced midlatitude open ocean. This setup creates a domain where mesoscale eddies dominate the flow field as they do at the OSMOSIS observation site in the North Atlantic [Buckingham *et al.*, 2016]. The model domain is a doubly periodic f plane of side length 256 km and depth 3700 m. There are 200 levels in the vertical with grid spacing that increases gradually from 3 m in the upper 90 m to 32.5 m in the deep interior. To investigate the causes of the filaments that arise in anticyclonic eddies in more detail, the model state from a simulation spun-up with 4 km horizontal grid resolution is interpolated to finer resolution 1 km and 0.25 km grids that permit submesoscale instabilities. The results of the experiment at the finest resolution **0.25 km grid** are the main focus of this paper.

The initial model state is derived from the fifth model year of the 4 km resolution simulation when the mean mixed layer depth is 35 m and the flow field has reached a statistically steady state [Brannigan *et al.*, 2015]. The particular time point chosen is when the model domain includes a well-resolved mesoscale cyclone and anticyclone that both have diameter of order 100 km (Figure S1 in the supporting information) and extend vertically over 1000 m into the thermocline (not shown). The cyclone and anticyclone are coherent vortex structures. The mesoscale anticyclone is the primary focus of this study.

The surface boundary condition is calculated relative to a uniform zonal 10 m wind speed of 6.3 m s^{-1} to allow eddy-Ekman interactions due to a relative wind stress [Gaube *et al.*, 2015]. The zonal wind stress gives rise to a southward Ekman transport in this Northern Hemisphere configuration. The surface boundary condition used here is simplified from that in Brannigan *et al.* [2015] where an additional spatially varying wind field provided an ongoing input of available potential energy. The simplified surface boundary condition used here means that the simulations are in a gradual “spindown” mode that is much slower than the timescale of days over which the filaments grow. Further simulations are carried out at resolutions of 4 km and 1 km where the surface frictional boundary condition is varied.

The surface heat flux for the base experiment is a cooling of 75 W m^{-2} though further simulations with no surface cooling are discussed. Boundary layer processes are parameterized using the K profile parameterization [Large *et al.*, 1994]. The numerical configuration is described in more detail in the supporting information.

The simulations use the biogeochemical package [Dutkiewicz *et al.*, 2005] of the MITgcm for a limiting nutrient experiment. This is a relatively simple biogeochemical package with just four tracer fields—dissolved inorganic carbon, alkalinity, phosphate, and dissolved organic phosphorus—and is used to test whether the temporal and depth scales over which the upwelling occurs can potentially lead to increased biological productivity even in highly oligotrophic conditions. The concentrations of the biogeochemical tracer fields are saturated with the exception of the limiting nutrient—phosphate—that is initialized in the thermocline 25 m below the base of the mixed layer. The biogeochemical package is also described in more detail in the supporting information.

2.2. Potential Vorticity

A novel feature of the analysis presented here is that the upwelling is tracked based on the Ertel potential vorticity

$$q = (f\mathbf{k} + \nabla \times \mathbf{u}) \cdot \nabla b, \quad (1)$$

where $f=10^{-4} \text{ s}^{-1}$ is the Coriolis parameter, \mathbf{k} is the vertical unit vector, ∇ is the gradient operator, $\mathbf{u} = (u, v, w)$ is the velocity vector, $b = -g\rho'/\rho_0$ is the buoyancy anomaly, $g = 9.81 \text{ m s}^{-2}$ is the gravitational acceleration, ρ' is potential density anomaly, and ρ_0 is the reference potential density. Horizontal gradients in the vertical velocity are everywhere negligible and so are excluded from the vorticity calculation.

To a first approximation, potential vorticity is low in the mixed layer due to weak stratification but is high in the thermocline due to strong stratification. The mixed layer potential vorticity decreases in the simulations due to the surface cooling. The potential vorticity is also reduced by the Ekman transport of heavier water over lighter water where the wind and geostrophic shear are aligned—a process referred to as “downfront” winds that extract potential vorticity from the ocean [Thomas, 2005]. However, the potential vorticity is increased by the

Ekman transport of lighter water over heavier water where the wind and geostrophic shear are opposed—a process referred to as “upfront” winds that input potential vorticity to the ocean [Thomas, 2005].

In the oligotrophic ocean, nutrients are depleted in the low-potential vorticity mixed layer but may be abundant in the high potential vorticity thermocline. Therefore, the presence of high potential vorticity fluid in the mixed layer is a strong indicator of upwelling that may increase biological productivity. A further advantage of tracking upwelling using potential vorticity is that the potential vorticity field provides important information about the stability of the flow and so allows rigorous testing of hypotheses for the physical process driving the upwelling.

2.3. Energetics

Adapting the approach of Thomas *et al.* [2013] to a vortex, the energetics that drive filament growth can be broken down into vertical buoyancy fluxes $\overline{w'b'}$, lateral shear production $\text{LSP} = -\overline{u'v'_r} \cdot \frac{\partial \mathbf{u}_b}{\partial r}$, and vertical shear production $\text{VSP} = -\overline{u'w'} \cdot \frac{\partial \mathbf{u}_b}{\partial z}$, where the overline denotes a spatial average over the anticyclone at a given depth, primes indicate perturbations as defined below, \mathbf{u}_b is the balanced vortex flow, v_r is the radial component of the vortex flow, and $\partial/\partial r$ is the derivative in the radial direction of the vortex. The balanced vortex flow is the simulation at 4 km at the corresponding time interpolated to the 0.25 km resolution grid, and the perturbations are defined as the difference between the simulation at 0.25 km resolution and the simulation interpolated from 4 km resolution.

3. Description of the Upwelling

At the mid-depth of the mixed layer in the anticyclone near the outset of the simulations (Figure 1a) there is positive potential vorticity in the south of the eddy due to the stratification induced by the southward Ekman transport of warmer fluid from closer to the eddy core over cooler fluid from further out in the eddy, consistent with numerical [Thomas, 2005] and observational results [D'Asaro *et al.*, 2011; Thomas *et al.*, 2013] from ocean fronts. This positive potential vorticity fluid is then carried to the western region of the eddy by the clockwise anticyclonic flow. However, as these fluid parcels move around to the northern region of the eddy, the potential vorticity changes from positive to negative (Figure 1a). This decrease in potential vorticity is due to the destratifying effect of the downfront Ekman transport in the north of the eddy that carries cooler fluid from the eddy periphery over warmer fluid closer to the eddy core. This southward Ekman transport weakens the stratification in the north of the eddy and so steepens the isopycnals toward the vertical. The weak stratification, negative relative vorticity, and strong horizontal buoyancy gradients in the north of the eddy give rise to negative potential vorticity (Figure S2). Fluid parcels with negative potential vorticity are then carried clockwise to the eastern region of the eddy.

Closer to the base of the mixed layer (Figure 1b), the negative potential vorticity that arises in the northern quadrant is found farther around the south of the eddy than at the mid-depth of the mixed layer (Figure 1a). This is because the restratification due to the Ekman transport in the south of the eddy is restricted to the Ekman layer in the upper 30 m, while the destratification in the north of the eddy extends deeper into the mixed layer [Thomas and Ferrari, 2008].

In the initial days of the simulation long filaments of thermocline fluid with high potential vorticity begin to emerge in the mixed layer of the eddy (Figures 1c–1f). The first filaments of positive potential vorticity fluid appear in the region of negative potential vorticity in the south and west of the eddy, for example, at (75, 70) km in Figure 1d. These positive potential vorticity filaments continue to grow as they are carried clockwise around the eddy, while new filaments emerge in regions of negative potential vorticity. A consistent feature of the upwelling process is that the high potential vorticity filaments do not follow paths of constant radius around the eddy but instead spiral in toward the center of the eddy, for example, at (100, 70) km in Figure 1f. Possible dynamical causes of this inward spiraling are discussed in section 5.

A useful signature of the upwelling is that it leads to cyclonic anomalies in the vertical component of relative vorticity at the surface (Movie S1). These cyclonic anomalies occur because fluid parcels are upwelled from the high stratification thermocline to the low stratification mixed layer and so the fluid parcels undergo strong vortex stretching.

In a vertical section through the eddy the upwelling forms a series of high potential vorticity filaments with low or negative potential vorticity filaments between them (for example in the north of the anticyclone from

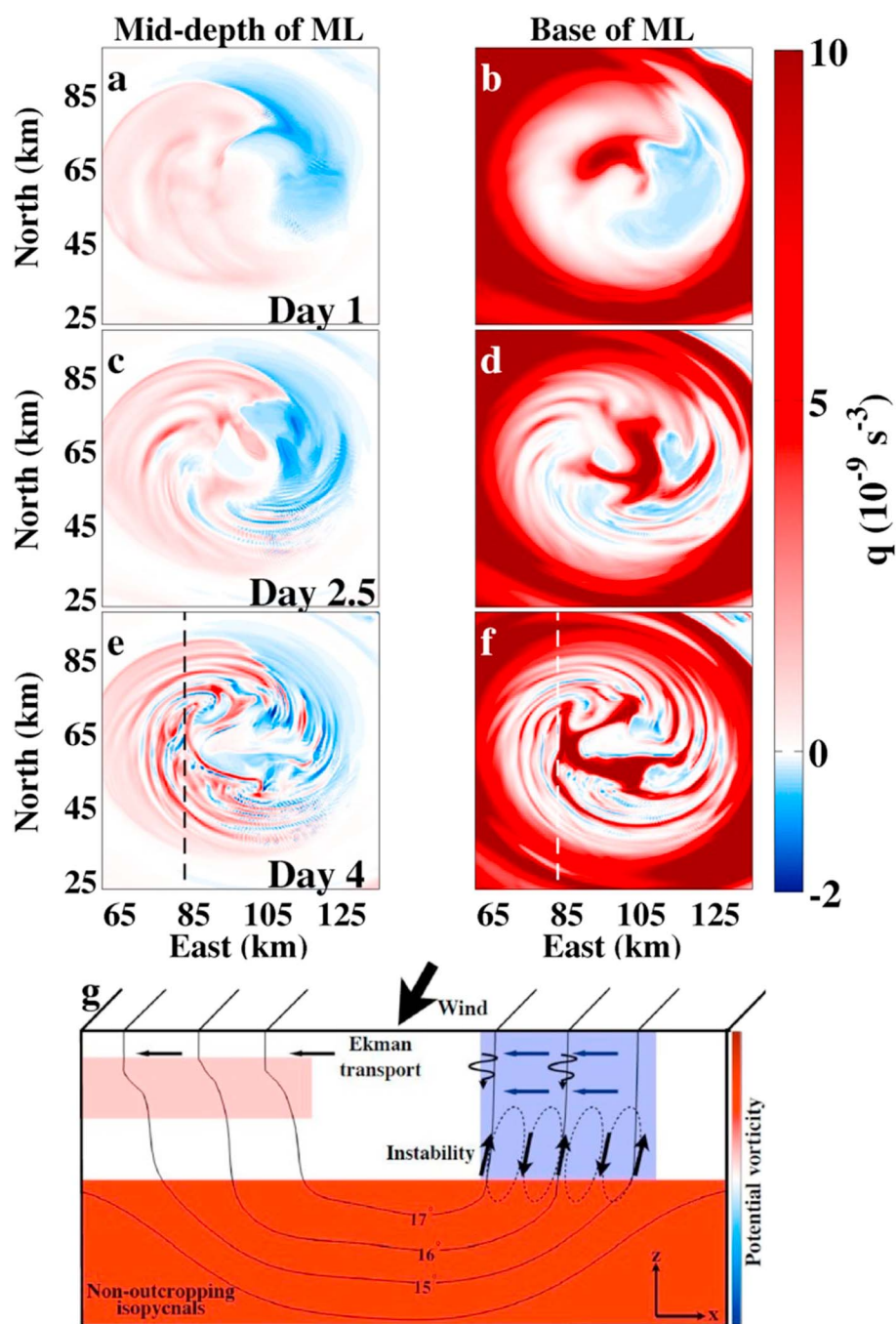


Figure 1. Potential vorticity at (a, c, and e) the mid-depth of the mixed layer (ML) at 26 m and at (b, d, and f) the base of the ML at 44 m. The dashed lines in Figures 1e and 1f are the location of the vertical slices in Figure 2 (a, b). The color scheme is saturated for positive values. (g) A schematic of the upwelling process with potential vorticity in color, isopycnals as solid lines, Ekman transport as horizontal arrows, vertical diapycnal mixing as curly arrows, and symmetric instability as the dashed streamlines with arrows.

70 km to 90 km in Figure 2a). The vertical sections confirm that the high potential vorticity filaments seen in the plan views in Figure 1 do indeed have a thermocline origin and so are carrying potentially nutrient-rich water toward the euphotic zone. The filaments are associated with large vertical velocities of 40 m d^{-1} (Figure 2b). The main energy source for the upwelling is a combination of vertical buoyancy fluxes and vertical shear production (Figure 2c). The experiment has been carried out with a range of surface boundary conditions that

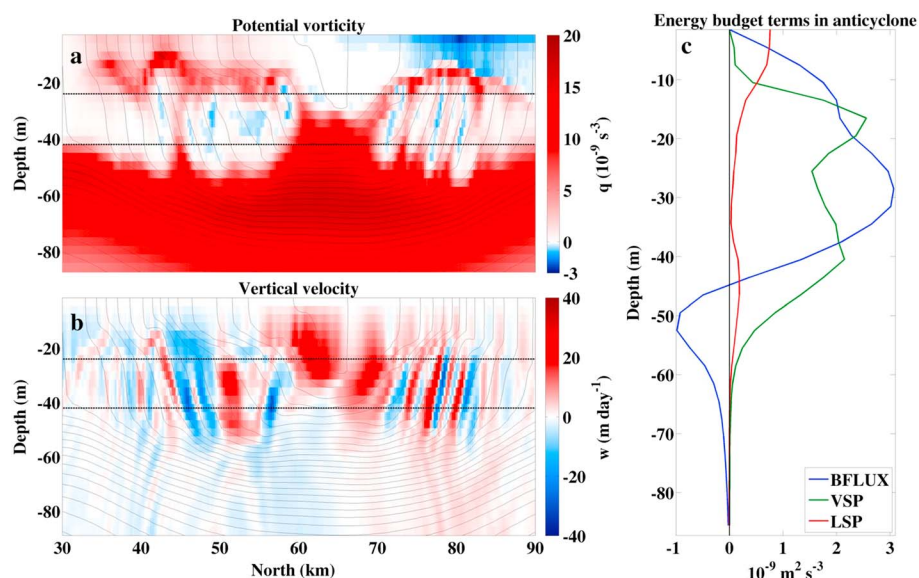


Figure 2. Vertical sections of (a) potential vorticity and (b) vertical velocity on the fourth day of the experiment with temperature contours of 0.2°C . Black dashed lines show the depths of the plan views in Figures 1e and 1f. (c) The components of the perturbation kinetic energy budget on the fourth day in the anticyclone.

all show similar qualitative results to the base experiment set out above, as discussed in more detail in the context of the limiting nutrient experiment in section 4 below.

This analysis focuses on the mesoscale anticyclone in the simulations as the anticyclone is where the strongest upwelling occurs. However, there is also wind-driven extraction of potential vorticity in the mesoscale cyclone. Upwelling of high potential vorticity fluid from the thermocline does occur in the cyclone but is restricted to a range of meters below the base of the mixed layer rather than tens of meters as in the anticyclone (not shown). The cyclone is overall more stable than the anticyclone, as values of potential vorticity are generally higher in the cyclone due to its positive relative vorticity and angular velocity, consistent with linear stability analysis of negative potential vorticity scenarios in barotropic cyclones and anticyclones [Smyth and McWilliams, 1998]. The instability in cyclones will be examined in more detail in a follow-on work.

3.1. Physical Cause of the Upwelling

The horizontal length scale of the upwelled filaments is of order 1 km (Figures 1e–1f) and so is well below the length scales that can be resolved in global climate models. In order to produce a parameterization for coarse resolution climate models the dynamical cause of the upwelling must be understood.

The upwelling due to a wind stress over a gradient in absolute vorticity [Stern, 1965; Mahadevan et al., 2008] has a dipole structure across an eddy [Gaube et al., 2015], while the upwelling due to a relative wind stress [Dewar and Flierl, 1987; McGillicuddy et al., 2007] is a monopole at the center of an eddy [Gaube et al., 2015]. In addition, the vertical velocities (Figure 2b) associated with the upwelling are 1 to 2 orders of magnitude larger than the vertical velocities from such eddy-wind interactions [Gaube et al., 2015]. Therefore, these eddy-wind interactions are not the cause of the upwelling. The wind forcing in the simulations is constant in time, and so high-frequency winds [Lévy et al., 2009] are not the cause of this upwelling. The entrainment of ambient mixed layer water into the eddy [Lehahn et al., 2011] is ruled out by the thermocline origin of the filaments.

Mixed layer baroclinic instability [Boccaletti et al., 2007; Omand et al., 2015] is rejected as the generating mechanism because the instability has a high cross-front wave number, whereas baroclinic instability is expected to result in a single overturning cell in the cross-front direction [Stone, 1966].

A process known as symmetric instability occurs for flows with potential vorticity that have the opposite sign to the Coriolis frequency f [Hoskins, 1974]—negative potential vorticity in this Northern Hemisphere case—due to the negative contribution of the horizontal components of potential vorticity [e.g., Thomas et al., 2013]. High-resolution numerical simulations of fronts show that symmetric instability in the mixed layer grows until it extends into the thermocline and upwells high potential vorticity fluid from the thermocline to

the mixed layer [Haine and Marshall, 1998; Thomas, 2005; Taylor and Ferrari, 2009] and has a high cross-front wave number [Stone, 1966]. Theoretical and numerical analyses show that symmetric instability is driven by a combination of vertical buoyancy fluxes and vertical shear production [Bachman and Taylor, 2014]. As the upwelling in these simulations is driven by a combination of vertical buoyancy fluxes and vertical shear production, occurs in a region of negative potential vorticity and has a high cross-front wave number, symmetric instability is taken to be the cause of the upwelling in the anticyclone. A schematic of the overall process is shown in Figure 1g.

4. Limiting Nutrient Experiment

The results in sections 3 and 3.1 show that there is transport of thermocline fluid into the mixed layer of the anticyclonic eddy due to symmetric instability. To test whether the simulated upwelling can potentially affect biological production in an oligotrophic environment, a simple limiting nutrient experiment is carried out. The limiting nutrient is initialized to be nonzero starting 25 m below the base of the mixed layer in the eddy, and so a vertical transport that extends well beyond the base of the mixed layer is required to transport the nutrient into the mixed layer. The deeper profile of the limiting nutrient compared to potential vorticity means that there is a lag between the initial growth of the high potential vorticity filaments and the biological response at the surface.

Biological activity is indeed found at the surface of the eddy in this limiting nutrient experiment (Figure 3a). The biological activity is highest around the core of the eddy, with a filament wrapping in toward the center at (85, 65) km at both the surface (Figure 3a) and the base of the mixed layer (Figure 3b). Such radially inward transport of nutrients may be a challenge for eddy centric compositing, as the process results in a radial distribution of biological activity that varies with time (Movie S1). While the filaments of high biological activity are relatively broad at the surface (Figure 3a), the filaments are sharper closer to the base of the mixed layer (Figure 3b). This is because shear dispersion induced by vertical shear and vertical diffusion increase the lateral dispersion of the limiting nutrient in the mixed layer. The high nutrient filaments are steeper than isopycnals due to the combined effect of advection and diffusion acting on the tracer field (Figure 3d).

There is also a transience to the nutrient upwelling. As the upwelling extends into the thermocline to transport nutrients into the mixed layer, this causes a concomitant deepening of the nutricline to a depth where eventually the filamentary upwelling is no longer active (Figure 3d). The upwelling pathways induced by the instability in the thermocline are aligned radially outward from the center of the eddy (Figure 3d). As such the radially inward transport in the mixed layer means that when nutrients eventually sink, a portion of the nutrients may be remineralized back into the upwelling region. This could allow some continuation of nutrient supply to the mixed layer. The strong transport of nutrients from the thermocline to the mixed layer by symmetric instability in an anticyclone is consistent with the results of Thomas *et al.* [2008] and Taylor and Ferrari [2011] for baroclinic fronts.

A range of surface boundary conditions are used to test the sensitivity of the upwelling (Figure 3e). Note that the surface biological productivity is similar at 1 km ("1 km base" in Figure 3e) and 0.25 km ("0.25 km base") resolutions, and both are much larger than that at 4 km resolution ("4 km base"). As such, the 1 km resolution simulation is used to test the sensitivity of the results to variations in the surface boundary condition.

A doubling of the surface wind speed ("1 km 2× wind" in Figure 3e) leads to a faster-developing instability and larger surface biological activity compared to the base experiment ("1 km base") as larger negative potential vorticity anomalies develop. On the other hand, imposing a uniform stress ("1 km stress") rather than a relative wind stress does not make a significant impact as the extraction of potential vorticity by downfront winds is similar in both cases.

With an anticyclonically rotating wind ("1 km anticyclonic" in Figure 3e) the biological activity grows faster than in the base experiment as part of the eddy experiences sustained downfront winds and thus larger negative potential vorticity anomalies occur. For a cyclonically rotating wind ("1 km cyclonic") the initial growth of the instability is slower compared to the base experiment. After a number of eddy rotation periods, however, the mean surface biological activity is similar between the base experiment and the experiments with either cyclonic or anticyclonic rotating winds because fluid parcels spend a similar amount of time in both the downfront and upfront regions irrespective of the rotation of the wind.

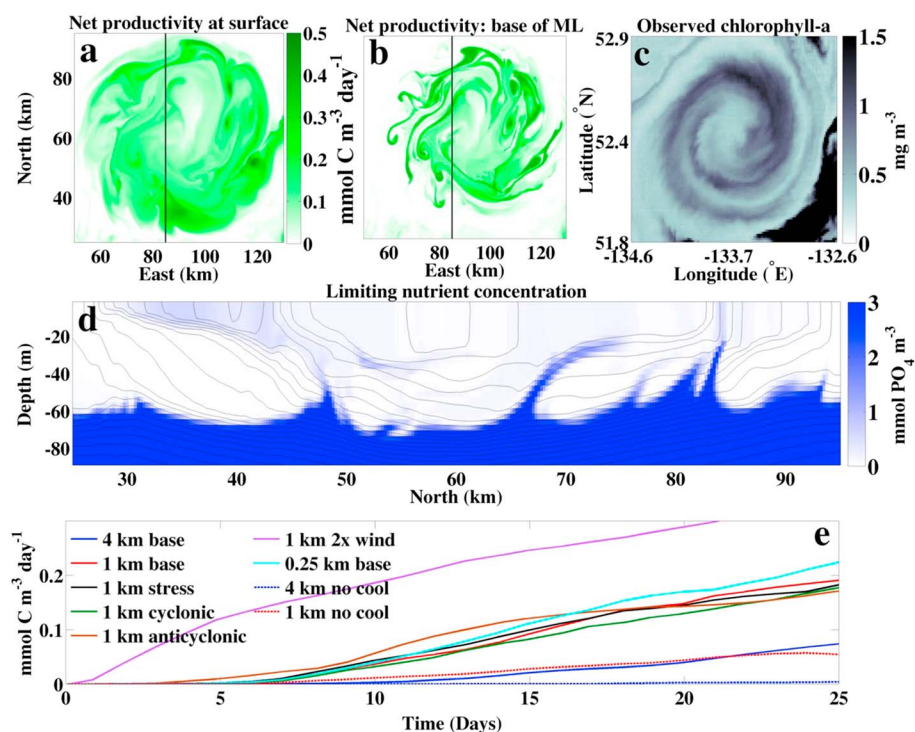


Figure 3. Net biological productivity on day 14 (a) at the surface and (b) at the base of the mixed layer at 29 m. The black lines in (Figures 3a and 3b) show where the vertical section in (Figure 3d) is taken. (c) Surface chlorophyll-a over a mesoscale anticyclonic eddy in the northeast Pacific Ocean on 15 June 2002. Provided by the NASA SeaWiFS program. (d) A vertical section of the limiting nutrient concentration with temperature contours of 0.2°C . (e) Surface productivity over the anticyclone with a range of surface boundary conditions and resolutions.

The magnitude of the surface biological activity is reduced for experiments with no surface cooling. However, while the surface biological activity falls almost to zero for the 4 km run with no cooling (“4 km no cool” in Figure 3e), the net effect is a reduction in surface biological activity by about half for the simulation with no cooling at 1 km (“1 km no cool”). The lower biological activity in these experiments reflects reduced extraction of potential vorticity at the surface, though there is also an experimental artifact in that the mixed layer shallows away from the limiting nutrient layer in these cases.

As the experiment is in a slow spindown mode, the primary result of the limiting nutrient experiment is that this upwelling pathway can lead to a significant increase in net productivity. It is cautioned, however, that the particular increase in productivity found here is almost certainly an overstatement of the change in biological activity that would be found in a steady state simulation that resolves basin-scale processes and included this upwelling pathway.

5. Discussion

The submesoscale length scale of the upwelling and the lack of a model parameterization for symmetric instability make it unlikely that this process is captured by existing mesoscale eddy-resolving models. As such, the symmetric instability mechanism is a new pathway for the transport of nutrients and dissolved gases between the mixed layer and thermocline of eddies that is not included in existing nutrient budgets for the ocean [Williams and Follows, 2011]. The large vertical velocities across the base of the mixed layer mean that symmetric instability in eddies may be an important factor in basin-wide nutrient budgets. An upper bound for the nutrient flux into the mixed layer may be calculated using the AVISO (Archiving, Validation and Interpretation of Satellite Oceanographic Data) delayed time global all-satellite gridded product. The area of anticyclonic eddies is estimated as the proportion of the Sargasso Sea with $\zeta^z < -5 \times 10^{-6} \text{ s}^{-1}$, where ζ^z is the vertical component of relative vorticity. The area of anticyclones is approximately 10% of the Sargasso Sea during May to August 2013. Following the approach of Williams and Follows [1998], the nitrogen flux across the mixed layer base due to symmetric instability in anticyclones can be

estimated as $wN \times A$ where an estimate of $w = 2.5 \text{ m d}^{-1}$ is half the root-mean-square vertical velocity at the base of the mixed layer based on the simulation at 1 km resolution with no surface cooling, $N = 10^{-3} \text{ mol N m}^{-3}$ is the nitrogen concentration at the base of the mixed layer [Fukumori *et al.*, 1991], and $A = 10\%$ is the proportion of the Sargasso Sea occupied by anticyclonic eddies in summer 2013. This gives an upper bound of about $0.1 \text{ mol N m}^{-2} \text{ yr}^{-1}$ that is comparable to other terms in the budget [Williams and Follows, 2011]. This estimate is an upper bound for net nutrient supply as it does not take into account the downwelling of nutrient-rich fluid from the mixed layer that would also be a consequence of symmetric instability. The residence timescale for fluid parcels in the mixed layer compared to the timescale of biological utilization is an important constraint that remains to be established.

An initial observational test can be made by comparing the model output with a remotely sensed anticyclone (Figure 3c). The regions of high chlorophyll-*a* concentration in the observed eddy have a filamentary character, and these filaments are wrapping into the eddy core. The image was taken on 12 June 2002 and has similar features to those observed by Hansen *et al.* [2010] or Godø *et al.* [2012]. Such a spatial distribution of chlorophyll-*a* would be consistent with the model predictions. Note that the chlorophyll-*a* image in Figure 3c is not a direct comparison for the model output (Figure 3a) as chlorophyll-*a* is a proxy for time-integrated net biological productivity, whereas the numerical results are a snapshot of net biological productivity. A full test of the hypothesis requires a comparison with high-resolution in situ data. From an observational perspective, the results here suggest that observations of mesoscale eddies that sample at the submesoscale are necessary. The sampling should be targeted toward the downfront wind region of the eddy where the Ekman transport acts to steepen isopycnals.

There are of course limitations to the symmetric instability mechanism as a route to higher primary productivity in eddies. A key constraint is that the source water for the eddy must be nutrient rich. The eddies with the highest nutrient concentrations are likely to be those that spin off from coastal currents [e.g., Gaube *et al.*, 2013]. In addition, biological productivity must be nutrient limited and so the upwelling mechanism would be less effective in light-limited regions in winter. A key point is that symmetric instability is likely to occur less often in periods of strong heating as restratification by solar heat fluxes competes against destratification by downfront winds [Thomas *et al.*, 2013]. As such upwelling due to symmetric instability may be strongest when solar insolation is weakest.

The simulations employed here are an idealized representation of the real ocean with simplified geometry and boundary conditions. The occurrence of symmetric instability is reduced due to reduced Eulerian vertical velocity shear when surface waves are aligned with the wind [Hamlington *et al.*, 2014; Haney *et al.*, 2015] but increased in anticyclonic flow by the horizontal component of planetary rotation [Colin de Verdière, 2012], and these effects are not included in the simulations. Evidence is emerging that interactions between symmetric instability and Langmuir circulation have nonlinear effects on tracer transports [Smith *et al.*, 2016]. The simulations presented here permit rather than resolve symmetric instability [Bachman and Taylor, 2014]. Simulations that fully resolve symmetric instability and its secondary shear instabilities require horizontal resolution that is still 2 orders of magnitude greater than employed here [Taylor and Ferrari, 2009]. Note that the energy budget from such large eddy simulations may have a smaller contribution from vertical buoyancy fluxes compared to shear production [Thomas and Taylor, 2010] due to restratifying modes of symmetric instability being preferentially resolved at coarser resolution [Bachman and Taylor, 2014].

The propensity for filaments to spiral into the core of the eddy is not a direct consequence of symmetric instability. A number of hypotheses can be proposed for the inward spiraling in the simulations including the straining effect of differential rotation [Methven and Hoskins, 1998] or submesoscale barotropic instabilities that grow on the reversals in lateral gradients of potential vorticity induced by the wind stress. The dynamical cause of the inward spiraling will be the subject of a follow-on work.

References

- Bachman, S., and J. Taylor (2014), Modelling of partially-resolved oceanic symmetric instability, *Ocean Modell.*, **82**, 15–27, doi:10.1016/j.ocemod.2014.07.006.
- Boccaletti, G., R. Ferrari, and B. Fox-Kemper (2007), Mixed layer instabilities and restratification, *J. Phys. Oceanogr.*, **37**(9), 2228–2250, doi:10.1175/JPO3101.1.
- Brannigan, L., D. Marshall, A. Naveira-Garabato, and G. Nurser (2015), The seasonal cycle of submesoscale flows, *Ocean Modell.*, **92**, 69–84.

Acknowledgments

The numerical simulations used in this paper are available on request from the author. This work was funded by the National Environment Research Council grants NE/I019921/1 as part of the OSMOSIS project, NE/F020252/1 as part of the DIMES project, and NE/I029633/1 as part of the TEA-COSI project. The simulations were carried out on the ARCHER UK National Supercomputing Service. The author thanks David Marshall, Alberto Naveira-Garabato, George Nurser, John Taylor, Andy Thompson, Dave Munday, Adrian Martin, Anna Rumyantseva, Lucy Tallents, and Jan Kaiser for helpful discussions. Scott Bachman, Ric Williams, and a further anonymous reviewer provided very constructive comments in the development of this work. The remotely sensed image was provided by NASA Ocean Biology (OB.DAAC). Sea-viewing Wide Field-of-view Sensor (SeaWiFS) Ocean Color Data, 2014.0 Reprocessing. NASA OB.DAAC, Greenbelt, MD, USA. doi:10.5067/ORBVIEW-2/SEAWIFS_OC.2014.0. Accessed on 2 October 2015.

- Buckingham, C., A. Naveira Garabato, L. Brannigan, A. F. Thompson, A. Lazar, D. Marshall, A. J. G. Nurser, G. M. Damerell, K. J. Heywood, and S. E. Belcher (2016), Seasonality of submesoscale flows in the ocean surface boundary layer, *Geophys. Res. Lett.*, **43**, doi:10.1002/2016GL068009.
- Colin de Verdière, Y. (2012), The stability of short symmetric internal waves on sloping fronts: Beyond the traditional approximation, *J. Phys. Oceanogr.*, **42**(3), 459–475.
- Crawford, W. R., P. J. Brickley, and A. C. Thomas (2007), Mesoscale eddies dominate surface phytoplankton in northern Gulf of Alaska, *Prog. Oceanogr.*, **75**(2), 287–303.
- D'Asaro, E., C. Lee, L. Rainville, R. Harcourt, and L. Thomas (2011), Enhanced turbulence and energy dissipation at ocean fronts, *Science*, **332**(6027), 318–322.
- Dewar, W. K. (1986), Mixed layers in Gulf Stream rings, *Dyn. Atmos. Oceans*, **10**(1), 1–29, doi:10.1016/0377-0265(86)90007-2.
- Dewar, W. K., and G. R. Flierl (1987), Some effects of the wind on rings, *J. Phys. Oceanogr.*, **17**(10), 1653–1667.
- Dietze, H., A. Oschlies, and P. Kähler (2004), Internal-wave-induced and double-diffusive nutrient fluxes to the nutrient-consuming surface layer in the oligotrophic subtropical North Atlantic, *Ocean Dyn.*, **54**(1), 1–7, doi:10.1007/s10236-003-0060-9.
- Dutkiewicz, S., A. Sokolov, J. Scott, and P. Stone (2005), A three-dimensional ocean-sea ice-carbon cycle model and its coupling to a two-dimensional atmospheric model: Uses in climate change studies, 47 pp., Joint Program on the Sci. and Policy of Global Change Tech. Mass. Inst. of Tech., Cambridge, Mass. [Available at <http://hdl.handle.net/1721.1/18091>.]
- Eden, C., and H. Dietze (2009), Effects of mesoscale eddy/wind interactions on biological new production and eddy kinetic energy, *J. Geophys. Res.*, **114**, C05023, doi:10.1029/2008JC005129.
- Franks, P. J., J. Wroblewski, and G. R. Flierl (1986), Prediction of phytoplankton growth in response to the frictional decay of a warm-core ring, *J. Geophys. Res.*, **91**(C6), 7603–7610.
- Fukumori, I., F. Martel, and C. Wunsch (1991), The hydrography of the North Atlantic in the early 1980s. An atlas, *Prog. Oceanogr.*, **27**(1–2), 1–110, doi:10.1016/0079-6611(91)90014-D.
- Gaube, P., D. B. Chelton, P. G. Strutton, and M. J. Behrenfeld (2013), Satellite observations of chlorophyll, phytoplankton biomass, and Ekman pumping in nonlinear mesoscale eddies, *J. Geophys. Res. Oceans*, **118**, 6349–370, doi:10.1002/2013JC009027.
- Gaube, P., D. B. Chelton, R. M. Samelson, M. G. Schlax, and L. W. O'Neill (2015), Satellite observations of mesoscale eddy-induced Ekman pumping, *J. Phys. Oceanogr.*, **45**(1), 104–132.
- Godø, O. R., A. Samuelsen, G. J. Macaulay, R. Patel, S. Hjøllø, J. Horne, S. Kaartvedt, and J. Johannessen (2012), Mesoscale eddies are oases for higher trophic marine life, *PLoS ONE*, **7**(1), e30161, doi:10.1371/journal.pone.0030161.
- Gruber, N., and J. L. Sarmiento (1997), Global patterns of marine nitrogen fixation and denitrification, *Global Biogeochem. Cycles*, **11**(2), 235–266.
- Haine, T. W. N., and J. Marshall (1998), Gravitational, symmetric, and baroclinic instability of the ocean mixed layer, *J. Phys. Oceanogr.*, **28**(4), 634–658.
- Hamlington, P. E., L. P. Van Roekel, B. Fox-Kemper, K. Julien, and G. P. Chini (2014), Langmuir-submesoscale interactions: Descriptive analysis of multiscale frontal spindown simulations, *J. Phys. Oceanogr.*, **44**(9), 2249–2272, doi:10.1175/JPO-D-13-0139.1.
- Haney, S., B. Fox-Kemper, K. Julien, and A. Webb (2015), Symmetric and geostrophic instabilities in the wave-forced ocean mixed layer, *J. Phys. Oceanogr.*, **45**, 3033–3056, doi:10.1175/JPO-D-15-0044.1.
- Hansen, C., E. Kvaleberg, and A. Samuelsen (2010), Anticyclonic eddies in the Norwegian Sea: Their generation, evolution and impact on primary production, *Deep Sea Res., Part I*, **57**(9), 1079–1091.
- Hoskins, B. J. (1974), Role of potential vorticity in symmetric stability and instability, *Q. J. R. Meteorol. Soc.*, **100**(425), 480–482.
- Jenkins, W. J., and J. C. Goldman (1985), Seasonal oxygen cycling and primary production in the Sargasso Sea, *J. Mar. Res.*, **43**(2), 465–491.
- Large, W. G., J. C. McWilliams, and S. C. Doney (1994), Oceanic vertical mixing—A review and a model with a nonlocal boundary-layer parameterization, *Rev. Geophys.*, **32**(4), 363–403.
- Lehahn, Y., F. D'Ovidio, M. Lévy, Y. Amitai, and E. Heifetz (2011), Long range transport of a quasi-isolated chlorophyll patch by an Agulhas ring, *Geophys. Res. Lett.*, **38**, L16610, doi:10.1029/2011GL048588.
- Lévy, M., P. Klein, and M. Ben Jelloul (2009), New production stimulated by high-frequency winds in a turbulent mesoscale eddy field, *Geophys. Res. Lett.*, **36**, L16603, doi:10.1029/2009GL039490.
- Mahadevan, A., L. N. Thomas, and A. Tandon (2008), Comment on "eddy/wind interactions stimulate extraordinary mid-ocean plankton blooms", *Science*, **320**(5875), 448, doi:10.1126/science.1152111.
- Marshall, J., A. Adcroft, C. Hill, L. Perelman, and C. Heisey (1997), A finite-volume, incompressible Navier Stokes model for studies of the ocean on parallel computers, *J. Geophys. Res.*, **102**(C3), 5753–5766.
- Martin, A. (2003), Phytoplankton patchiness: The role of lateral stirring and mixing, *Prog. Oceanogr.*, **57**(2), 125–174, doi:10.1016/S0079-6611(03)00085-5.
- McGillicuddy, D. J., et al. (2007), Eddy/wind interactions stimulate extraordinary mid-ocean plankton blooms, *Science*, **316**(5827), 1021–1026.
- Methven, J., and B. Hoskins (1998), Spirals in potential vorticity. Part I: Measures of structure, *J. Atmos. Sci.*, **55**(11), 2053–2066.
- Michaels, A. F., N. R. Bates, K. O. Buesseler, C. A. Carlson, and A. H. Knap (1994), Carbon-cycle imbalances in the Sargasso Sea, *Nature*, **372**(6506), 537–539.
- Omand, M. M., E. A. D'Asaro, C. M. Lee, M. J. Perry, N. Briggs, I. Cetinic, and A. Mahadevan (2015), Eddy-driven subduction exports particulate organic carbon from the spring bloom, *Science*, **348**(6231), 222–225.
- Shulenberger, E., and J. L. Reid (1981), The Pacific shallow oxygen maximum, deep chlorophyll maximum, and primary productivity, reconsidered, *Deep Sea Res., Part A*, **28**(9), 901–919.
- Smith, K. M., P. E. Hamlington, and B. Fox-Kemper (2016), Effects of submesoscale turbulence on ocean tracers, *J. Geophys. Res. Oceans*, **121**, 908–933, doi:10.1002/2015JC011089.
- Smyth, W., and J. McWilliams (1998), Instability of an axisymmetric vortex in a stably stratified, rotating environment, *Theor. Comput. Fluid Dyn.*, **11**(3–4), 305–322, doi:10.1007/s001620050095.
- Stern, M. E. (1965), Interaction of a uniform wind stress with a geostrophic vortex, *Deep Sea Res. Oceanogr. Abstr.*, **12**, 355–367, Elsevier.
- Stone, P. H. (1966), On non-geostrophic baroclinic stability, *J. Atmos. Sci.*, **23**(4), 390–400.
- Taylor, J. R., and R. Ferrari (2009), On the equilibration of a symmetrically unstable front via a secondary shear instability, *J. Fluid Mech.*, **622**, 103, doi:10.1017/S0022112008005272.
- Taylor, J. R., and R. Ferrari (2011), Ocean fronts trigger high latitude phytoplankton blooms, *Geophys. Res. Lett.*, **38**, L23601, doi:10.1029/2011GL049312.
- Thomas, L., and R. Ferrari (2008), Friction, frontogenesis, and the stratification of the surface mixed layer, *J. Phys. Oceanogr.*, **38**(11), 2501–2518, doi:10.1175/2008JPO3797.1.

- Thomas, L. N. (2005), Destruction of potential vorticity by winds, *J. Phys. Oceanogr.*, *35*(12), 2457–2466.
- Thomas, L. N., and J. R. Taylor (2010), Reduction of the usable wind-work on the general circulation by forced symmetric instability, *Geophys. Res. Lett.*, *37*, L18606, doi:10.1029/2010GL044680.
- Thomas, L. N., A. Tandon, and A. Mahadevan (2008), Submesoscale processes and dynamics, in *Ocean Modeling in an Eddying Regime*, edited by M. W. Hecht and H. Hasumi, pp. 17–38, AGU, Washington, D. C.
- Thomas, L. N., J. R. Taylor, R. Ferrari, and T. M. Joyce (2013), Symmetric instability in the Gulf Stream, *Deep Sea Res., Part II*, *91*, 96–110, doi:10.1016/j.dsr2.2013.02.025.
- Williams, R. G., and M. J. Follows (1998), The Ekman transfer of nutrients and maintenance of new production over the North Atlantic, *Deep Sea Res., Part I*, *45*(2–3), 461–489, doi:10.1016/S0967-0637(97)00094-0.
- Williams, R. G., and M. J. Follows (2011), *Ocean Dynamics and the Carbon Cycle: Principles and Mechanisms*, Cambridge Univ. Press, pp. 267–276, Cambridge, U. K.
- Yentsch, C. S., and D. A. Phinney (1985), Rotary motions and convection as a means of regulating primary production in warm core rings, *J. Geophys. Res.*, *90*(C2), 3237–3248.